ISA Transactions 129 (2022) 558–571

Contents lists available at ScienceDirect

ISA Transactions

journal homepage: www.elsevier.com/locate/isatrans

Practice article

Torque ripple attenuation of PMSM using improved robust two-degree-of-freedom controller via extended sliding mode parameter observer

Mingfei Huang [a,b], Yongting Deng [a,*], Hongwen Li [a], Jianli Wang [a]

[a] Changchun Institute of Optics, Fine Mechanics, and Physics, Chinese Academy of Science, Changchun 130033, China
[b] The University of Chinese Academy of Sciences, Beijing 100049, China

ARTICLE INFO

Article history:
Received 27 August 2021
Received in revised form 25 January 2022
Accepted 29 January 2022
Available online 7 February 2022

Keywords:
Extended sliding-mode parameter observer
Iterative learning control
Permanent magnet synchronous motor
Two-degree-of-freedom internal model control

ABSTRACT

Torque ripple caused by flux harmonics, nonlinearity of inverter and current measurements decreases the accuracy of the servo control system, which limits the application of permanent magnet synchronous motor (PMSM) with high precision requirement. To reduce torque ripple, this paper proposes an improved robust two-degree-of-freedom controller (IR-2DOFC) based on an extended sliding-mode parameter observer (ESMPO) for a PMSM. The IR-2DOFC is constructed around the 2DOFC with iterative learning control (ILC) and a series-connecting structure, which not only suppresses unmodeled disturbances and periodic components, but also attenuates the negative impact of ILC on the dynamic response. Meanwhile, to improve the robust stability of the IR-2DOFC, ESMPO identifies the mechanical parameters so that they can be employed to further establish the IR-2DOFC parameters. Additionally, the observed disturbances can be regarded as a feed-forward compensation component to the IR-2DOFC, which enhances the disturbance-rejection performance. Simulations and experiments show that the IR-2DOFC with ESMPO has an improved dynamic response performance, which exhibits better robustness with respect to internal and external load disturbances and harmonics torque compared with proportional–integral (PI) and PI-ILC controllers.

1. Introduction

Permanent magnet synchronous motor (PMSM) has been widely used in fields of robotics, elevators, and aerospace, owing to its advantages of compact structure, high-power density, and wide speed range [1–5]. However, the challenges of parameter perturbations, system uncertainties, external load disturbances, and nonlinear properties decrease its regulation performance [6–9]. As such, the traditional proportional–integral–derivative (PID) controller has limited ability to handle multiple-source disturbances and cannot achieve satisfactory control performance for high-precision applications.

To improve the control performance, various control methods have been designed for speed and current-loop performance improvements, such as active disturbance rejection control (ADRC) [10,11], model predictive control (MPC) [12,13], and fuzzy neural control (FNC) [14,15]. Compared with the PID controller, ADRC provides a novel way to suppress disturbances and realizes good transient trajectories by introducing the extended-state observer and a noise reduction differentiator. However, this requires a complex design law that limits its application to industry. MPC is an advanced control strategy that provides a candidate for electrical drives designed around cost-function optimization. The MPC can handle multivariable constraints while ensuring satisfactory robustness and dynamic response. However, the weight coefficient used in the MPC is difficult to determine [16]. FNC has shown success in parameter tuning of the controllers, forecasting tools, and operator approximation, because it presents an option for users to interpret unknown models. Nevertheless, for controller design, the robust stability of an FNC is difficult to guarantee. Apart from these control strategies, adaptive, observer-based, and sliding-mode controls were offered in [17–19]. Generally, these advanced nonlinear controllers can enhance the control performance in different ways, but some rely on ideal assumptions and large computational requirements [20] that reduce their utility. Thus, the conventional cascading control structure can still be considered for PMSM.

Robust two-degree-of-freedom controller (2DOFC) provides a practical approach for PMSM drive systems, because it decouples the dynamic response and robustness using two internal mode filters, which not only realize good dynamic response according to a preset tracking trajectory, but they also achieve satisfactory robustness to uncertain and external disturbances [21–27].

* Corresponding author.
E-mail address: dengyongting@ciomp.ac.cn (Y. Deng).

https://doi.org/10.1016/j.isatra.2022.01.033
0019-0578/

In [21], a 2DOFC for a direct-current (DC) motor was proposed, and its effectiveness was validated through experiments. In [25], the nonlinear electrical dynamics of PMSM were considered for the 2DOFC design, and the derived condition provided an idea for determining 2DOFC parameters. Because many 2D OFC controllers have been proposed in the literature [24,27], this type of controller can effectively suppress the slow-time varying disturbances of PMSM by setting an appropriate bandwidth for its filter. However, disturbances caused by harmonic torque are difficult to suppress, because the disturbance model does not reside in the controller's forward channel. The torque ripple can be reduced by setting a larger bandwidth for the controller, but it may cause the control system to be more sensitive to noise [21].

To reject the repetitive disturbances, several control methods have been developed. Owing to periodic disturbances, repetitive control (RC) has been developed to compensate for the torque ripple. RC is simple and reliable, but the converge rate of the steady-state error caused by periodic input is slow. In [28], the multiple resonant control (MRC) scheme was proposed to suppress torque ripple. MRC can effectively suppress periodic disturbances, but it can only reject disturbances at known frequencies. In [29], an observer-based control method was presented to eliminate torque ripple from various sources. This methodology has advantages of light computation burden and fewer information requirements for periodic disturbances, although nonlinear factors are not considered.

An alternate control strategy for periodic disturbance is the iterative learning control (ILC), which is based on the internal mode principle and has the technical advantages of small computation burden and easy implementation [30–32]. Therefore, it is widely employed to handle the periodic disturbance rejection problem. In [33], a PI based ILC controller (PI-ILC) is proposed to minimized the torque ripple of PMSM. The structure of this control method is simple, and it has significant effect to minimize the speed harmonics. However, the non-periodic disturbance is not considered, which cannot be suppressed by the ILC; In addition, it should be pointed out that the ILC will result in awful transition process with high overshoot and oscillation before iterative error converging [34], which decreases the control performance. To improve the dynamic response, the adaptive PI-ILC controllers have been developed in [35–37], which can adjust the convergence rate and dynamic performance of the system. However, due to the delay of weight calculation, the stability and robust stability of the system are difficult to ensure.

To avoid these drawbacks and achieve satisfactory robustness to repetitive disturbance, this paper extends the 2DOFC structure to the periodic case, and suppresses the torque ripple (i.e., IR-2DOFC). It is worth noting that the non-DC uncertainties and constant disturbances are both undesirable for PMSM control system. Hence, the proposed control approach takes advantages of the traditional 2DOFC and an ILC based disturbance compensation term, which can reject both non-periodic and periodic disturbances. Different from the ILC-based controller, which has a parallel connection structure [35–40], a series-connect structure is designed that is simpler and more straightforward. The undesired dynamic response caused by ILC can be removed by using the series-connect structure and 2DOFC. Meanwhile, to ensure the robust stability condition derived from the small gain theorem, an ESMPO is constructed to estimate the mechanical parameters and enables the nominal model involved in the design of IR-2DOFC to approach the real control plant as close as possible. Furthermore, the estimated disturbance can be added in the control loop to further enhance the anti-disturbance capability. Finally, an observer-based IR-2DOFC scheme is explored, which can improve the control performance of PMSM in terms of dynamic response, robustness to uncertain disturbance and suppression capacity for torque ripple. Simulation and experimental are carried out to verify the correctness of the proposed controller.

Based on the above analysis, this article is organized as follows: the overview of mathematical model of PMSM and the design guideline of the traditional 2DOF controller are provided in Section 2. Section 3 presents the design process and performance analysis of the developed control method. Section 4 shows the optimal design of the IR-2DOFC with ESMPO. Section 5 provides the simulation and experimental results, respectively. Our conclusions are then presented in Section 6.

2. Mathematical model of PMSM and review of the traditional 2DOF controller

2.1. Mathematical model of PMSM

The vector control model based on coordinate transformation can be expressed as follows [5]

$$\begin{cases} u_q = R_n I_q + L_{nq}\dot{I}_q + p\omega_m(L_{nq}I_d + \Psi_f) \\ u_d = R_n I_d + L_{nd}\dot{I}_d - p\omega_m L_{nq} I_q \end{cases} \tag{1}$$

where u_d, u_q, I_d, I_q, L_{nd} and L_{nq} are the voltages, currents and inductances along d-q axis, respectively; R_n is the resistance; p is number of pole pares, and ω_m denotes the mechanical angular frequency; Ψ_f is the flux linkage.

Then, the dynamic equation of PMSM can be expressed as

$$J\dot{\omega}_m = T_e\text{-}B\omega_m\text{-}T_L \tag{2}$$

in which $T_e = 1.5p[\Psi_f I_q - (L_{nd} - L_{nq})I_d I_q]$ is the electromagnetic torque; If the surface-mounted structure ($L_{nd} = L_{nq} = L_n$) is employed for PMSM, T_e can be further simplifies $T_e = 1.5p\Psi_f i_q$; J and B are the inertial and frictional coefficient, respectively; T_L is the external load torque.

Based on Laplace transformation, the transfer function between input and output of the PMSM can be expressed as

$$\omega_m(s) = (T_e\text{-}T_L)P(s) \tag{3}$$

where $P(s) = 1/(Js + B)$ is the controlled plant.

2.2. Review of the traditional 2DOF controller

The feedback controller $C_A(s)$ and detector $C_B(s)$ form the 2DOF controller, which provides preset dynamic responses and satisfactory robustness to uncertain external disturbances. According to the 2DOF control principle described in [21], the two components can be expressed as

$$\begin{cases} C_A(s) = Q_1(s)/[P_n(s)(1 - Q_1(s))(1 - Q_2(s))] \\ C_B(s) = Q_2(s)/[P_n(s)(1 - Q_2(s))] \end{cases} \tag{4}$$

where $Q_1(s) = 1/(\lambda s + 1)$ and $Q_2(s) = (2\tau s + 1)/((\tau s)^2 + 2\tau s + 1)$ represent the internal model filters, which determine the dynamic response and robust performance of the controller; $P_n(s) = 1/(J_n s + B_n)$ is the nominal model of control plant (see Fig. 1).

When the controlled plant is accurate i.e., $P(s) = P_n(s)$, the transfer function of the speed loop using 2DOFC can be expressed

$$\omega(s) = Q_1(s)\omega_{ref}(s) + P(s)(1 - Q_2(s))(1 - Q_1(s))d(s) \tag{5}$$

It can be observed from Eq. (5) that the transfer function $Q_1(s)$ corresponding to the dynamic response is decoupled from the disturbance suppression term $(1 - Q_2(s))(1 - Q_1(s))$, which shows the advantage of the 2DOFC. If the robust term $(1 - Q_2(s))(1 - Q_1(s))$ ensures enough transient decay rate, then the disturbance

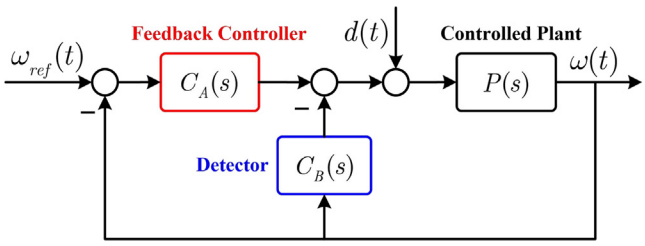

Fig. 1. Control diagram of the traditional 2DOFC.

can be rejected. The suppression performance depends on the decay bandwidth; when the λ and τ are chosen such that $\lambda \gg \tau$, the 2DOFC can achieve a certain ability to suppress these disturbances. On the other hand, the control performance is allowed to balance between the disturbance rejection and noise suppression. Therefore, a trade-off tuning of the parameters between practical design constraints and robustness should be made in the 2DOFC scheme.

3. Design of the IR-2DOF controller

To further improve the control performance of the traditional 2DOFC, especially that of the suppression performance for periodic disturbance, this paper proposes a hybrid robust control strategy that combines the 2DOF controller with ILC to provide a series connection structure. The negative impact caused by ILC can be rejected by the series-connecting structure and 2DOF controller, which guarantees the desire dynamic response. Then, the ESMPO is established to obtain the nominal model of the control plant and further minimize the disturbances caused by various sources.

3.1. Reformulation of the 2DOF controller

To make a clearer statement of this part, some frequency characteristics of these filters are defined:

$$\begin{cases} |Q_1(s)|_{s=j\omega} = \begin{cases} 1 \cdots \omega \le \omega_{c1} \\ 0 \cdots \omega > \omega_{c1} \end{cases} \\ |Q_2(s)|_{s=j\omega} = \begin{cases} 1 \cdots \omega \le \omega_{c2} \\ 0 \cdots \omega > \omega_{c2} \end{cases} \end{cases} \tag{6}$$

where ω_{c1} and ω_{c2} are the corresponding cut off frequency of the $Q_1(s)$, $Q_2(s)$, which satisfies $\omega_{c1} < \omega_{c2}$.

The IR-2DOFC is developed based on the traditional 2DOFC and ILC, which, together, has the following form:

$$\begin{bmatrix} A_{LC}(s) \\ B_{LC}(s) \end{bmatrix} = \begin{bmatrix} C_A(s) & 0 \\ 0 & C_B(s) \end{bmatrix} \begin{bmatrix} L(s) \\ L(s) \end{bmatrix} \tag{7}$$

where $A_{LC}(s)$ and $B_{LC}(s)$ represent the modified controllers; $L(s)$ is the embedded ILC controller in the two channels.

The traditional ILC method in the frequency domain can be expressed as [31]

$$L(s) = \phi/(1 - \alpha e^{-\xi s}) \tag{8}$$

where ϕ is the learning gain, α is the forgetting factor, and $\xi = 2\pi/\omega_m$ is the iterative cycle period. To guarantee the convergence of the iterative error, a sufficient and necessary condition for the choice can be given as $\alpha \le 1$ [37].

If the ILC is embedded in the 2DOFC, the Laplace transformation of the speed loop can be expressed as

$$\begin{aligned} \omega(s) =& Q_1(s)L(s)\omega_{ref}(s)/T(s) \\ &+ (1 - Q_1(s))(1 - Q_2(s))P(s)d(s)/T(s) \end{aligned} \tag{9}$$

where $T(s)$ is the characteristic polynomial of a closed loop, and can be denoted as $T(s) = (1 - Q_1(s))(1 - Q_2(s)) + (Q_1(s) + (1 - Q_1(s))Q_2(s))L(s)$.

In order to analyze the frequency characteristic of $T(s)$, $T(s)$ is rewritten as

$$T(s) = 1 - [Q_1(s) + (1 - Q_1(s))Q_2(s)][1 - L(s)] \tag{10}$$

It is not difficult to verify that $|1 - L(s)|_{s=j\omega} = 0$ when $|L(s)|_{s=j\omega} = 1$, then Eq. (9) can be expressed as

$$\begin{aligned} \omega(s) =& Q_1(s)\omega_{ref}(s) \\ &+ (1 - Q_1(s))(1 - Q_2(s))P(s)d(s)/T(s) \end{aligned} \tag{11}$$

Eq. (11) indicates the speed can perfectly track the command value when $L(s)$ strictly satisfied $|L(s)|_{s=j\omega} = 1$. However, the ILC is a scheme used to deal with repetitive signal. It is thus the ILC cannot maintain enough gain at the DC frequency ($\omega < \omega_{cl}$) i.e., $|L(s)|_{s=j\omega} \ll 1$, and the speed tracking becomes $Q_1(s)L(s)\omega_{ref}(s)$ changing the preset dynamic response. Additionally, the ILC will produce a high gain in the middle-high frequency band ($\omega_{c1} < \omega < \omega_{c2}$), i.e., $|L(s)|_{s=j\omega} \gg 1$; Meanwhile, $Q_1(s)$, $Q_2(s)$ satisfies $|(1 - Q_1(s))Q_2(s)| = |Q_2(s)| = 1 \gg |Q_1(s)|$ in this frequency range. It is thus the speed tracking can be yielded as $Q_1(s)L(s)\omega_{ref}(s)/(1+L(s))$, which is affected by the ILC.

To overcome this drawback, the ILC should be modified as a series-connecting structure

$$\begin{bmatrix} A_{LC}(s) \\ B_{LC}(s) \end{bmatrix} = \begin{bmatrix} C_A(s) & 0 \\ 0 & C_B(s) \end{bmatrix} \begin{bmatrix} L(s)+1 \\ L(s)+1 \end{bmatrix} \tag{12}$$

Replacing $L(s)$ with $L(s) + 1$, the characteristic polynomial can be yielded as

$$T'(s) = 1 + [Q_1(s) + (1 - Q_1(s))Q_2(s)][L(s)] \tag{13}$$

Then, the closed loop transfer function can be modified as

$$\begin{aligned} \omega(s) =& Q_1(s)(L(s)+1)\omega_{ref}(s)/T'(s) \\ &+ (1 - Q_1(s))(1 - Q_2(s))P(s)d(s)/T'(s) \end{aligned} \tag{14}$$

where $T'(s) = 1 + [Q_1(s) + (1 - Q_1(s))Q_2(s)]L(s)$.

Generally, the controller works in the low and middle-high frequencies. Hence, the amplitude response of the controller is analyzed in these frequency bands. When the controller is in the DC frequency, i.e., $\omega < \omega_{cl}$, it is simple to verify that $|L(s)| \ll |Q_1(s)| = 1$, the characteristic polynomial $T'(s)$ is approximately equal to $T'(s) = 1$. Then, the speed tracking term $Q_1(s)(L(s)+1)\omega_{ref}(s)/T'(s)$ can be considered as $Q_1(s)\omega_{ref}(s)$, hence the motor can still guarantee a satisfactory dynamic response. When the controller is in the middle-high frequency band i.e., $\omega_{c1} < \omega < \omega_{c2}$, we can conclude that $|L(s)| \gg |(1 - Q_1(s))\, Q_2(s)| = |Q_2(s)| = 1 \gg |Q_1(s)|$, $T'(s)$ becomes $T'(s) = 1 + L(s)$, the speed tracking term can still be $Q_1(s)\omega_{ref}(s)$, which can ensure an excellent transition process. It can be observed that the dynamic response is maintained as the frequency-domain characteristic of a first-order link in the two frequency bands. It is thus the IR-2DOFC can track the command value with the expected regulation performance.

Meanwhile, according to Eq. (14), the robust term of the controller is given by

$$R(s) = (1 - Q_1(s))\,(1 - Q_2(s))\,P(s)d(s)/(1 + L(s)) \tag{15}$$

Assuming the disturbance existing in speed loop is expressed as

$$d(s) = d_{DC}(s) + d_{re}(s) \tag{16}$$

where $d_{DC}(s)$ and $d_{re}(s)$ represents the slow-time varying and repetitive disturbances.

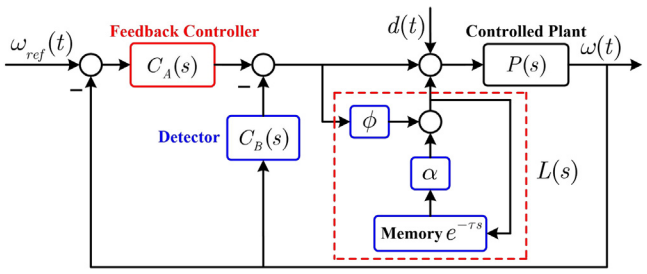

Fig. 2. Control diagram of the IR-2DOFC.

The $d_{DC}(s)$ can be rejected by setting the cutoff frequency of $(1-Q_1(s))(1-Q_2(s))$ larger than $d_{DC}(s)$, then this kind of frequency can be easily minimized. Furthermore, the periodic components $d_{re}(s)$ can be suppressed by using $(1+L(s))^{-1}$ because this term appears attenuation characteristics at these frequency points. This indicates the IR-2DOFC has the ability to suppress both the DC and periodic disturbances.

Analysis mentioned above shows that the transfer function corresponding to the dynamic response is decoupled from the embedded series-connecting ILC, providing a better transition process. Meanwhile, the improved 2DOFC can further suppress periodic components by leveraging the ILC. Therefore, the IR-2DOFC controller has an improved performance while minimizing torque ripples and providing satisfactory robustness to slow time varying disturbances, which shows the advantage of the proposed controller. According to Eq. (12), the control diagram of the IR-2DOFC is illustrated in Fig. 2.

3.2. Design of the IR-2DOFC

To design the IR-2DOFC, an *H-infinity* synthesis of the IR-2DOFC is provided, and the obtained conditions are employed to form the system constraints.

The closed-loop transfer function of speed is provided as follows:

$$\begin{aligned}\omega(s) =& \frac{C_A(s)(1+L(s))P(s)}{1+P(s)\left(C_A(s)+C_B(s)\right)(1+L(s))}\omega_{ref}(s)\\ &+\frac{P(s)d(s)}{1+P(s)\left(C_A(s)+C_B(s)\right)(1+L(s))}\end{aligned} \tag{17}$$

Theorem 1 (*Stability*)**.** *The speed loop with IR-2DOFC is asymptotically stable if and only if the ILC satisfies the following condition:*

$$\|L(s)\|_\infty < \left\| \frac{|1+P(s)\left(C_A(s)+C_B(s)\right)|}{P(s)\left(C_A(s)+C_B(s)\right)} \right\|_\infty \tag{18}$$

in which $\|\cdot\|_\infty$ *is the infinity norm of the transfer function.*

Proof. Before analysis of the stability of the IR-2DOFC, the stability of the tradition 2DOFC controller should be introduced. The coprime fraction description $U_{IMC}(s)$ of the 2DOFC can be expressed as

$$\begin{cases} P(s) = N(s)\Xi^{-1}(s) \\ U_{IMC}(s) = [C_B(s),\, C_A(s)+C_B(s)] \\ \qquad\quad = \Xi_c^{-1}(s)\,[K_1(s),\, K_2(s)]\,; \end{cases} \tag{19}$$

where $N(s)=1$; $\Xi^{-1}(s)=P_n(s)$; $K_1(s)=(1-Q_1(s))Q_2(s)$; $K_2(s)=(1-Q_1(s))Q_2(s)+Q_1(s)$; ${\Xi_c}^{-1}(s)=[P_n(s)(1-Q_1\,(s))(1-Q_2(s))]^{-1}$.

According to stability analysis in [21], the control loop with 2DOFC is internally stable if and only if $\Xi(s)$, $\Xi_c(s)$, $N(s)$, and $K_2(s)$ satisfy the following condition:

$$\Xi_c(s)\Xi(s)+N(s)K_2(s)=1 \tag{20}$$

Substituting Eq. (19) into Eq. (20), it is not difficult to verify that this condition can be held, because the 2DOF controller is stable.

When the series-connected ILC is embedded into the 2DOFC, the closed-loop-characteristic polynomial can be expressed as

$$\begin{aligned}\Psi(s) =& 1+P(s)(C_A(s)+C_B(s))(1+L(s))\\ =& [1+P(s)(C_A(s)+C_B(s))]\\ &\times\ \left[1+\frac{P(s)(C_A(s)+C_B(s))L(s)}{1+P(s)(C_A(s)+C_B(s))}\right]\\ =& [1+P(s)(C_A(s)+C_B(s))]\\ &\times\ [1+\theta(s)]\end{aligned} \tag{21}$$

where $\theta(s)$ is the closed gain produced by ILC.

Assuming the condition in Eq. (20) is satisfied, the stability of the IR-2DOFC controller is only determined by the following transfer function:

$$\theta(s) = \frac{P(s)\left(C_A(s)+C_B(s)\right)L(s)}{1+P(s)\left(C_A(s)+C_B(s)\right)} \tag{22}$$

Based on small gain theorem represented in [41], the closed loop with IR-2DOFC is stable if and only if the following condition is met:

$$\|\theta(s)\| \le \left\| \frac{P(s)\left(C_A(s)+C_B(s)\right)}{1+P(s)\left(C_A(s)+C_B(s)\right)} \right\|_\infty \|L(s)\| < 1 \tag{23}$$

It is therefore apparent that Eq. (18) can be derived from Eq. (23). The condition in Eq. (18) shows that the open gain of ILC cannot be designed to be as large. According to the analysis in [37], a larger forgetting factor α can obtain better torque ripple suppression performance. It is however this will result in more significant accumulative effect of non-periodic disturbance contained in the signal i.e., $|L(s)|$ is more closed to 1 in the low frequency band, which decrease the dynamic response. Hence, this paper suggests α is firstly selected a value to have certain torque ripple suppression performance (minimum steady-state error) and guarantee small amplitude gain in DC frequency band ($|L(s)| \ll 1$). And then, the learning gain ϕ should be set a large enough value to ensure a high gain in high frequency band ($|L(s)| \gg 1$), while meeting the stability condition.

Theorem 2 (*Robust Stability*)**.** *When the model error is considered in the speed loop, and the control plant can be expressed as* $P_\Delta(s) = (\Delta_P(s)+P_n(s))$*, we assume that the conditions of Eqs. (18) and (20) are satisfied, and the speed loop has robust stability if the following condition is held:*

$$\|\Delta_P(s)\|_\infty < \left\| \frac{1}{P(s)\left(C_A(s)+C_B(s)\right)(1+L(s))} \right\|_\infty \tag{24}$$

Proof. The characteristic polynomial, $\Psi(s)$ with $P_\Delta(s)$ is expressed as follows:

$$\begin{aligned}&\tilde{\Psi}(s)\\ =& 1+P(s)(1+\Delta_P(s))\times(C_A(s)+C_B(s))(1+L(s))\\ =& [1+P(s)(C_A(s)+C_B(s))(1+L(s))]\\ &\times\ \left[1+\frac{P(s)(C_A(s)+C_B(s))(1+L(s))}{1+P(s)(C_A(s)+C_B(s))(1+L(s))}\Delta_P(s)\right]\\ =& \Lambda(s)(1+\Omega(s)\Delta_P(s))\end{aligned} \tag{25}$$

where $\Lambda(s) = 1+P(s)(C_A(s)+C_B(s))(1+L(s))$, $\Omega(s) = \frac{P(s)(C_A(s)+C_B(s))(1+L(s))}{1+P(s)(C_A(s)+C_B(s))(1+L(s))}$.

According to the stability property analysis, it is not difficult to find that $\Lambda(s)$ can be stabilized by satisfying Eqs. (18) and (20). Therefore, to guarantee the robust stability of $\tilde{\Psi}(s)$,

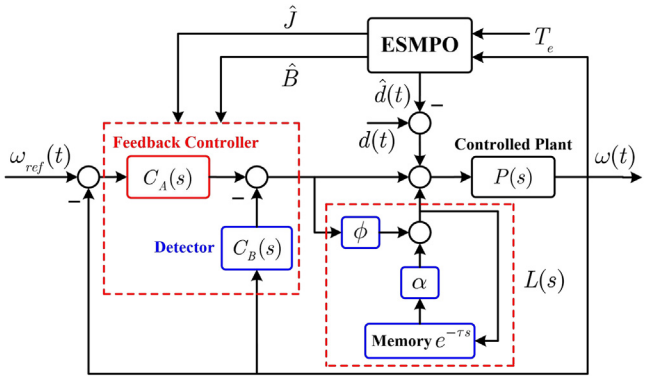

Fig. 3. Control diagram of the IR-2DOFC via ESMPO.

$(1 + \Omega(s)\Delta_P(s))$ should be stable. Based on the small gain theorem [40], a sufficient condition for the robust stability of a closed-loop system can be expressed as

$$\left\|\Omega(s)\Delta_p(s)\right\| \le \|\Omega(s)\| \left\|\Delta_p(s)\right\| < 1 \tag{26}$$

This implies that

$$\begin{aligned} &\|\Delta_P(s)\|_\infty \\ &< \left\| \frac{1 + P(s)\,(C_A(s) + C_B(s))\,(1 + L(s))}{P(s)\,(C_A(s) + C_B(s))\,(1 + L(s))} \right\|_\infty \\ &< \|P(s)\,(C_A(s) + C_B(s))\,(1 + L(s))\|_\infty \\ &\quad \cdot \left\| \frac{1 + \frac{1}{P(s)(C_A(s)+C_B(s))(1+L(s))}}{P(s)\,(C_A(s) + C_B(s))\,(1 + L(s))} \right\|_\infty \\ &< \left\| \frac{1}{P(s)\,(C_A(s) + C_B(s))\,(1 + L(s))} \right\|_\infty \end{aligned} \tag{27}$$

According to Eq. (27), the robust stability condition of Eq. (24) can be obtained. Furthermore, as can be observed from Eq. (27), reducing the model error between the control plant and the nominal plant can enhance the robust stability. Thus, to improve the robust stability of the IR-2DOFC, ESMPO is introduced, which estimates the parameters of the control plant and ensures that the nominal plant is as close as possible to the actual model.

4. Optimal design of the IR-2DOFC with ESMPO

It can be observed from Eq. (4) that the establishment of IR-2DOFC is based on the model of the control plant. Hence, to obtain the mechanism parameters of PMSM, ESM PO is designed to distinguish these parameters and further compensate for the multiple sources of disturbance. The overall control diagram of the proposed control method is illustrated in Fig. 3.

4.1. Design of the ESMPO

Assume that the nominal model of the control plant and the actual model has the following linear equation:

$$(J_n + \Delta J)\dot{\omega}_m = T_e\text{-}(B_n + \Delta B)\omega_m\text{-}T_L \tag{28}$$

where J_n and B_n are the initial moments of inertia and the viscous friction coefficient, respectively, which can be considered to be the nominal model of the controlled plant. T_L represents the external load. The two mechanical parameters can be obtained by prior knowledge. ΔJ and ΔB denote the model errors occurring between the actual parameters and crude estimations.

Based on Eqs. (2) and (28), the dynamic model having lumped uncertainty and disturbance can be described as

$$\begin{cases} J_n\dot{\omega}_m = T_e\text{-}B_n\omega_m\text{-}d \\ d = \Delta J\dot{\omega}_m\text{+}\Delta B\omega_m\text{+}T_L \end{cases} \tag{29}$$

where d represents the lumped uncertainty and external disturbance.

In the PMSM drive system, the sampling frequency of the speed loop is much higher than the change rate of the disturbance d. Thus, the first derivative of the lumped uncertainty and the external disturbance d can be considered to be $\dot{d}(t) = 0$.

Combining Eq. (29) and $\dot{d}(t) = 0$, the following extended state-space equation is obtained:

$$\begin{cases} \begin{bmatrix} \dot{\omega}_m \\ \dot{d} \end{bmatrix} = \begin{bmatrix} -B_n/J_n & -1/J_n \\ 0 & 0 \end{bmatrix} \begin{bmatrix} \omega_m \\ d \end{bmatrix} + \begin{bmatrix} 1/J_n \\ 0 \end{bmatrix} T_e \\ \omega_m = \begin{bmatrix} 1 & 0 \end{bmatrix} \begin{bmatrix} \omega_m \\ d \end{bmatrix} \end{cases} \tag{30}$$

Then, the extended sliding observer can be established as follows [42]:

$$\begin{aligned} \begin{bmatrix} \dot{\hat{\omega}}_m \\ \dot{\hat{d}} \end{bmatrix} &= \begin{bmatrix} -B_n/J_n & -1/J_n \\ 0 & 0 \end{bmatrix} \begin{bmatrix} \hat{\omega}_m \\ \hat{d} \end{bmatrix} \\ &\quad + \begin{bmatrix} 1/J_n \\ 0 \end{bmatrix} T_e\text{+} \begin{bmatrix} \vartheta_1(s_\omega) \\ \vartheta_2(s_\omega) \end{bmatrix} \end{aligned} \tag{31}$$

where $\hat{\omega}_m$ denotes the estimated mechanical angular velocity, $\hat{d}$ represents the estimated disturbance $\vartheta_1(s_\omega)$ and $\vartheta_2(s_\omega)$ are the sliding mode control laws, and s_ω is the integral sliding surface used to eliminate the steady state error and achieve precise speed control, which can be given as

$$s_\omega = e_\omega + c\int_0^t e_\omega dt \tag{32}$$

where $c > 0$ is the integral constant, and $e_\omega = \omega_m - \hat{\omega}_m$ denotes the observed error of mechanical angular velocity.

Based on SMC theory, $\vartheta_1(s_\omega)$ and $\vartheta_2(s_\omega)$ can be expressed as

$$\begin{cases} \vartheta_1(s_\omega) = (c - \dfrac{B_n}{J_n})e_\omega + g(k_\omega, \xi, s_\omega)sign(s_\omega) \\ \vartheta_2(s_\omega) = -Lg(k_\omega, \xi, s_\omega)sign(s_\omega) \end{cases} \tag{33}$$

where $sign(.)$ is the switch function; $L > 0$ is the observed gain that can ensure the observed error converge to zero; $g(k_\omega, \xi, s_\omega) > 0$ is the variable-gain coefficient adopted to reduce the chattering phenomenon of SMC, which can be given as [19]

$$g(k_\omega, \xi, s_\omega) = k_\omega/[\xi + (1 + 1/|s_\omega| - \xi)exp(-\delta|s_\omega|)] \tag{34}$$

in which k_ω is the switch gain; $0 < \xi < 1$ is a parameter that can reduce the chattering when system trajectory approaches the sliding-mode surface; $\delta > 0$ denotes the exponential decay rate; $exp(\cdot)$ is the exponential function.

By combining (30) and (31), the observed error of speed and disturbance can be yielded as follows:

$$\begin{bmatrix} \dot{e}_\omega \\ \dot{e}_d \end{bmatrix} = \begin{bmatrix} -B_n/J_n & -1/J_n \\ 0 & 0 \end{bmatrix} \begin{bmatrix} e_\omega \\ e_d \end{bmatrix} + \begin{bmatrix} -\vartheta_1(s_\omega) \\ -\vartheta_2(s_\omega) \end{bmatrix} \tag{35}$$

where $e_d = d - \hat{d}$ is the estimated error of disturbance.

In order to analysis the stability of the ESMPO, the following Lyapunov function is introduced and given as

$$V = \frac{1}{2}s_\omega^2 \tag{36}$$

Differentiating V with respect to t we can obtain.

$$\begin{aligned} \dot{V} &= s_\omega\dot{s}_\omega = s_\omega(-\vartheta_1(s_\omega) - B_n e_\omega/J_n\text{+}ce_\omega - e_d/J_n) \\ &= s_\omega[-e_d/J_n - g(k_\omega, \xi, s_\omega)sign(s_\omega)] \end{aligned} \tag{37}$$

In order to ensure the finite-time Lyapunov stability theory, the derivative of V should satisfy the condition $\dot{V} < 0$, that requires

$$s_\omega[-(g(k_\omega, \xi, s_\omega))sign(s_\omega) - e_d/J_n] < 0 \tag{38}$$

where $g(k_\omega, \xi, s_\omega) \approx k_\omega/\xi$ is the switch gain when the sliding mode surface is far away from the equilibrium point.

Thus, to ensure the tracking trajectory reach the sliding mode surface in a finite time, k_ω and ξ should be selected such that

$$\frac{k_\omega}{\xi} > \left|\frac{e_d}{J_n}\right| \tag{39}$$

Once the k_ω and ξ are set as Eq. (39), the space trajectory of the observer can reach the sling surface and remain on it. Meanwhile, the switch gain becomes $g(k_\omega, \xi, s_\omega) \approx k_\omega |s_\omega| / [(|s_\omega| + 1)]$, which can suppress the chattering of SMC.

Furthermore, the speed error satisfies $e_\omega = \dot{e}_\omega = 0$ [19]. Substituting this equation into Eq. (35) can derive the following result

$$\begin{cases} e_\omega = \dot{e}_\omega = -g(k_\omega, \xi, s_\omega)sign(s_\omega) - e_d/J_n = 0 \\ \dot{e}_d = Lg(k_\omega, \xi, s_\omega)sign(s_\omega) \end{cases} \tag{40}$$

Thus, we can obtain the following equation

$$\frac{\dot{e}_d}{L} = \frac{-e_d}{J_n} \tag{41}$$

Integrating both sides of the equation with respect to time t, we can achieve the following result

$$e_d = \frac{-L}{J_n}\int_0^t \dot{e}_d dt = \chi exp(\frac{-L}{J_n}t) \tag{42}$$

where χ is an integral constant.

Noting that $J_n > 0$, it is simple to observe that the estimated error will converge to zero as time t tends to infinity when L is selected in the range of $L > 0$. Thus, the observer can precisely observe the disturbance existing in the control system, and the estimated result will also converge to the actual value.

4.2. Inertial parameter estimation

During the estimating process, a simple PI controller is designed to regulate the speed. When estimating the inertia of the PMSM, the command speed runs in a constant acceleration, C_a and a deceleration operation $-C_d$. The minus sign indicates the deceleration, which can be expressed as follows:

$$\begin{cases} \hat{d}(t) = \Delta J\dot{\omega}_{m1}(t) + \Delta B\omega_{m1}(t) + T_L \\ \quad\quad = \Delta JC_a + \Delta B\omega_{m1}(t) + T_L \\ \hat{d}(t+T_1) = \Delta J\dot{\omega}_{m1}(t+T_1) + \Delta B\omega_{m1}(t+T_1) + T_L \\ \quad\quad = -\Delta JC_d + \Delta B\omega_{m1}(t+T_1) + T_L \end{cases} \tag{43}$$

where T_1 is the interval between two different operating conditions.

Given that $\omega_{m1}(t) = \omega_{m1}(t+T_1)$, we can obtain

$$\hat{d}(t+T_1) - \hat{d}(t) = \Delta J(C_a + C_d) \tag{44}$$

It can be observed from Eq. (44) that the ESMPO can identify the inertia even when the viscous friction coefficient is not precisely known. Then, the inertial error can be expressed as

$$\Delta J = (\hat{d}(t+T_1) - \hat{d}(t))/(C_a + C_d) \tag{45}$$

It is assumed that the parameters needed during parameter identification are $0 \sim iT_1$, and the values of C_a and C_d satisfy $C_d = C_a = C$. To simplify the notation, acceleration and deceleration are noted as acceleration in this paper, then the actual inertial value can be further simplified as

$$\Delta J = (\hat{d}(t+T_1) - \hat{d}(t))/2C \tag{46}$$

Thus, the actual value of inertia can be given as

$$J = \Delta J + J_n \tag{47}$$

4.3. Viscous friction coefficient estimation

To identify parameter$B$, the PMSM should work during zero-acceleration at different speeds. When the PMSM runs at its first steady-state speed $\omega_{m2}(t)$, for an interval of T_2 based on Eq. (29), the observed disturbance can be expressed as

$$\begin{cases} \hat{d}(t) = \Delta J\dot{\omega}_{m2}(t) + \Delta B\omega_{m2}(t) + T_L \\ \hat{d}(t+T_2) = \Delta J\dot{\omega}_{m2}(t+T_2) + \Delta B\omega_{m2}(t+T_2) + T_L \end{cases} \tag{48}$$

Owing to the fact that the PMSM operates in a zero-acceleration state, we can obtain $\dot{\omega}_{m2}(t) = \dot{\omega}_{m2}(t+T_2) = 0$. Thus, Eq. (48) can be rewritten as

$$\begin{cases} \hat{d}(t) = \Delta B\omega_{m2}(t) + T_L \\ \hat{d}(t+T) = \Delta B\omega_{m2}(t+T_2) + T_L \end{cases} \tag{49}$$

According to Eq. (49), the estimation of B can be further expressed as

$$\begin{cases} \Delta B = (\hat{d}(t+T_2) - \hat{d}(t))/(\omega_{m2}(t+T_2) - \omega_{m2}(t)) \\ B = B_n + \Delta B \end{cases} \tag{50}$$

Based on the analysis described above, the designed ES MPO can identify the mechanism parameters and can be used to optimize the IR-2DOFC design. Meanwhile, the ESMPO can enhance the disturbance rejection performance by estimating the load disturbance while compensating it online. The overall process of the parameter estimation is shown in Fig. 4.

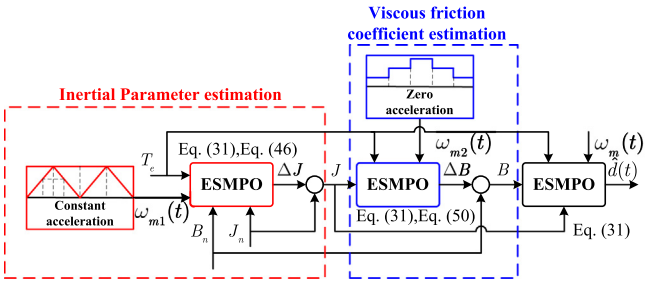

Fig. 4. The flow chart of parameter estimation.

Table 1
Parameters of PMSM.

Symbol	Quantity	Value and unit
L	d–q frame inductance	0.0085 H
R	Armature resistance	0.569 Ω
P	Number of pole pairs	3
f	Flux linkage	0.035 Wb
J	Inertia	0.098 kg m^2
T_R	Rated torque	10 N m
S_R	Rated speed	250 rpm
I_R	Rated current	7:00 AM
P_w	Nominal power	5.5 kW
B	Viscous friction coefficient	0.00185 N m s/rad

5. Simulation and experimental verifications

To verify the effectiveness of the proposed control strategy, simulations and experiments were conducted using the MATLAB/Simulink. Table 1 lists the parameters of the PMS M prototype.

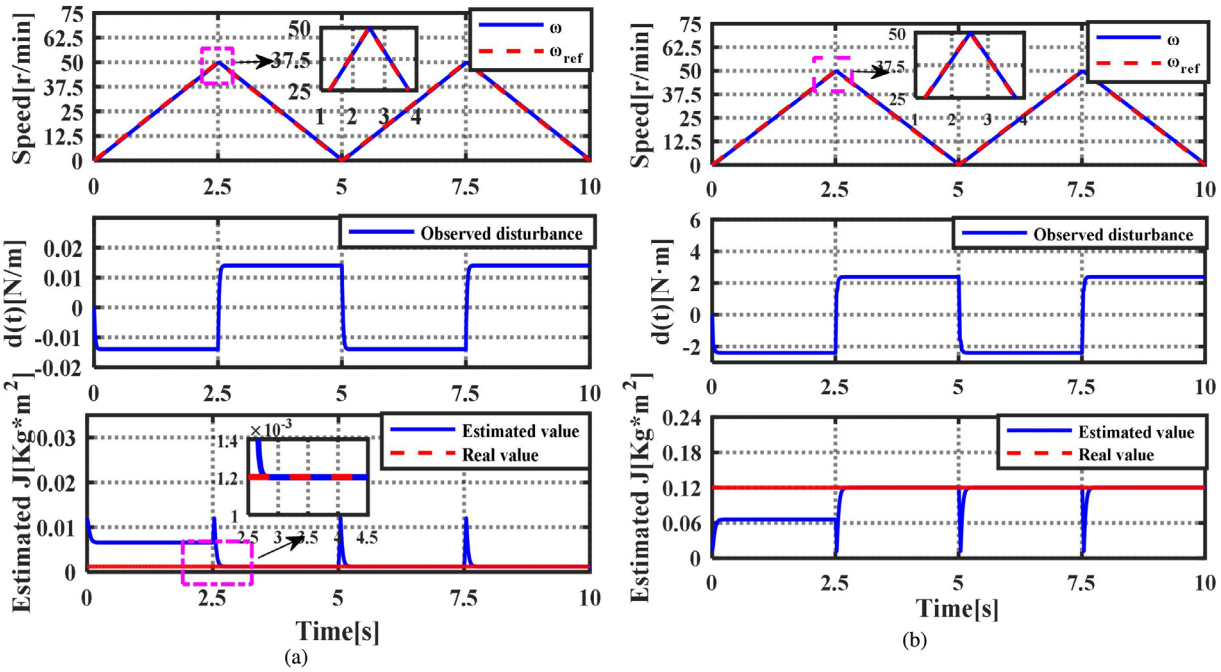

Fig. 5. Simulation results of inertial estimation with an acceleration of 1200 rpm^2: (a) inertial estimation of $J = J_n/10$; (b) inertial estimation of $J = 10J_n$.

5.1. Simulation verification

5.1.1. Parameter estimation

The simulation verification of the proposed control strategy is performed in the MATLAB/Simulink (Version: R201 6b). It should be noted that the optimal IR-2DOFC cannot be established without the ESMPO; hence, the parameter estimation is performed using a non-optimal PI controller ($k_p = 20J_n$, $k_i = 20B_n$) first in the speed loop; where J_n and B_n are the initial parameters to design the ESMPO. The other parameters of the ESMPO are set as $k_\omega = 38\,000$, $c = 100$, $L = 30\,000$, $\xi = 0.7$ and $\delta = 100$, respectively. The intervals of T_1 and T_2 used for ESMPO are set to 2.5 and 2 s, respectively, and the acceleration is determined to be 1200 rpm^2. Fig. 5 illustrates the simulation results of the inertial estimation with $J = 10J_n$ and $J = J_n/10$. It is worth noting that the J_n and B_n remains fixed, and the parameters is only changed in the controlled plant. It can be seen that the inertial error can be estimated based upon the disturbance observed by the ESMPO. Hence, the real value of inertia can be calculated past an interval of T_1. Fig. 6 demonstrates the viscous friction coefficient estimating results as it changes from $B = B_n/10$ to $B = 10B_n$. It can be observed that the ESMPO ensures that the estimated value converges to the actual value by setting different speeds at the range of $iT_2 \sim (i+1)T_2$, where i indicates the ith interval with zero acceleration. After the precise parameters are estimated, the IR-2DOFC is constructed using an optimized manner. Then, the ESMPO can be considered to be a disturbance and provide it as a feed-forward value to the IR-2DOFC.

5.1.2. Dynamic response evaluation

To highlight the proposed control method in terms of dynamic response, PI and PI-ILC [37] controllers are employed for comparison. Using the previous parameter identification, the optimal PI controller [28] can be redesigned as follows:

$$i_{ref} = (k_p + \frac{k_i}{s})(\omega_{ref} - \omega_m(t)) \tag{51}$$

where $k_p = \rho J$, $k_i = \rho B$ and ρ is a parameter that determines the bandwidth of the PI controller, which is associated with the settling time and disturbance suppression. J and B are the observed values from the ESMPO.

To guarantee an equitable evaluation, the PI controller and the IR-2DOFC are tuned to obtain a transient process having a fixed settling time, which indicates $\rho_0 = \lambda^{-1}$. For example, ρ_0 and λ are set as 20 and 0.05, respectively. The forgetting factor α, and the learning gain ϕ of the ILC are designated as 0.85 and 0.7, respectively.

Fig. 7(a) demonstrates the transition process of the PI-ILC with different ρ_0. The optimal PI controller (blue trace) can ensure the speed reaches the command value with the setting time of 0.2 s without overshoot. When the ILC controller is used in speed loop, the trajectory (red trace) has the oscillation resulting an overshoot of 16%, which extends the setting time to reach the steady-state. The dynamic response can be improved by setting a smaller ρ_0; however, the bandwidth is decreased, and the disturbance suppression is reduced. Therefore, the traditional PI controller has difficulty balancing the dynamic response and the disturbance suppression performance.

By comparing IR-2DOFC to PI-ILC, it provides better transition regulation performance. it can be observed that the worst dynamic response with IR-2DOFC has the overshoot of 0.97%, and the setting time is 0.267 s, which shows little change. Meanwhile, it is worth noting that the tracking performance can be optimized by tuning the $|\tau - \lambda|$ term to a large value with a fixed setting time, which exemplifies the advantage of the proposed controller.

5.1.3. Disturbance suppression evaluation with external load

To validate the disturbance suppression performance of the proposed control method, an external load of 1 N m was acted upon the motor. It can be observed from Fig. 8(a) that the speed with the PI controller had a large vibration and could not track the reference speed during the load process. When the proposed controller was used in the speed loop, the speed showed little change; meanwhile, the speed could retrace the given value precisely and quickly. Fig. 8(b) illustrates the observed torque from the ESMPO, where it can be seen that the ESMPO estimated the external load and was used as a feed-forward component to reject disturbances.

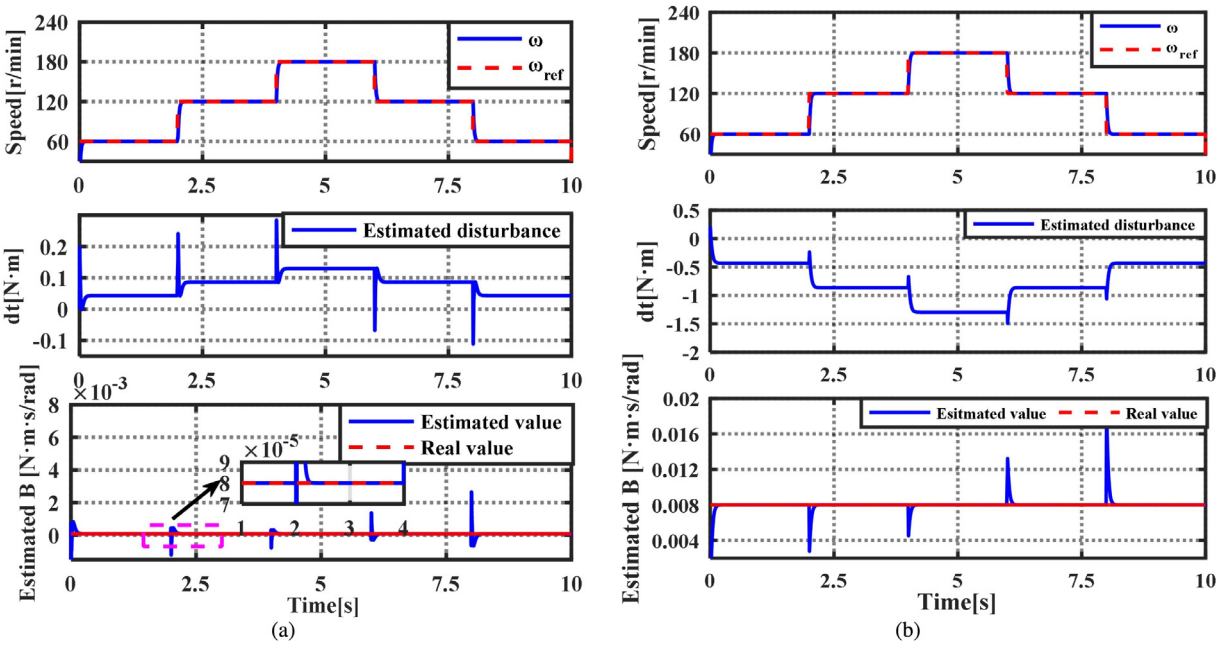

Fig. 6. Simulation results of viscous friction coefficient estimation with a speed step of ±60 rpm: (a) viscous friction coefficient estimation of $B = B_n/10$; (b) viscous friction coefficient estimation of $B = 10B_n$.

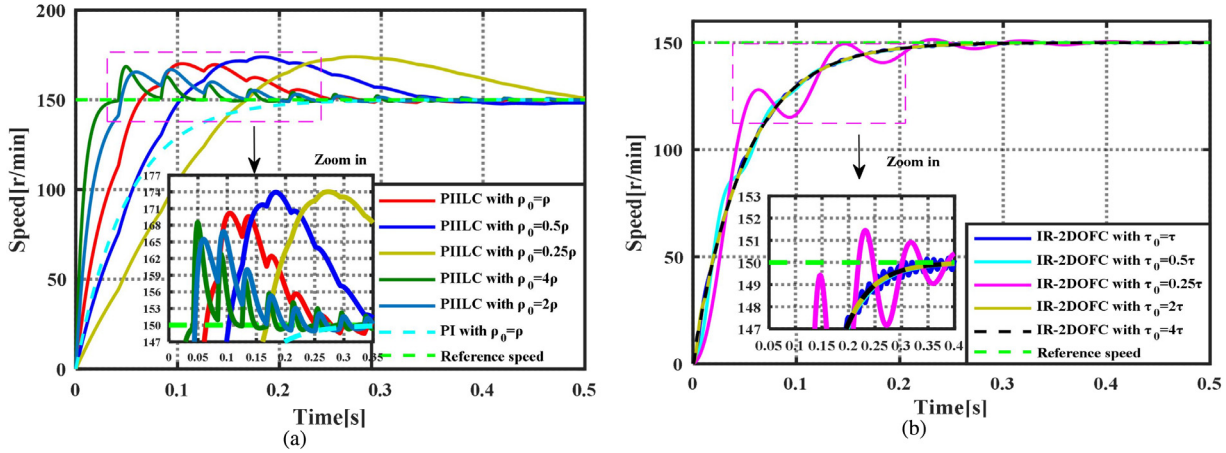

Fig. 7. Step response comparisons of PI-ILC and IR-2DOFC: (a) step response of PI-ILC with different values of ρ_0; (b) step response of IR-2DOFC with different values of τ. (For interpretation of the references to color in this figure legend, the reader is referred to the web version of this article.)

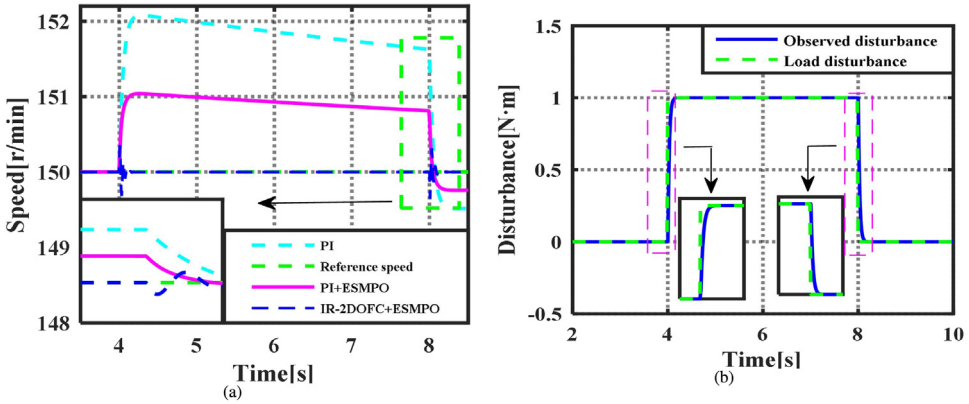

Fig. 8. Disturbance suppression evaluation: (a) simulation results of speed steady-state performance with sudden load; (b) curves of observed load disturbances with ESMPO.

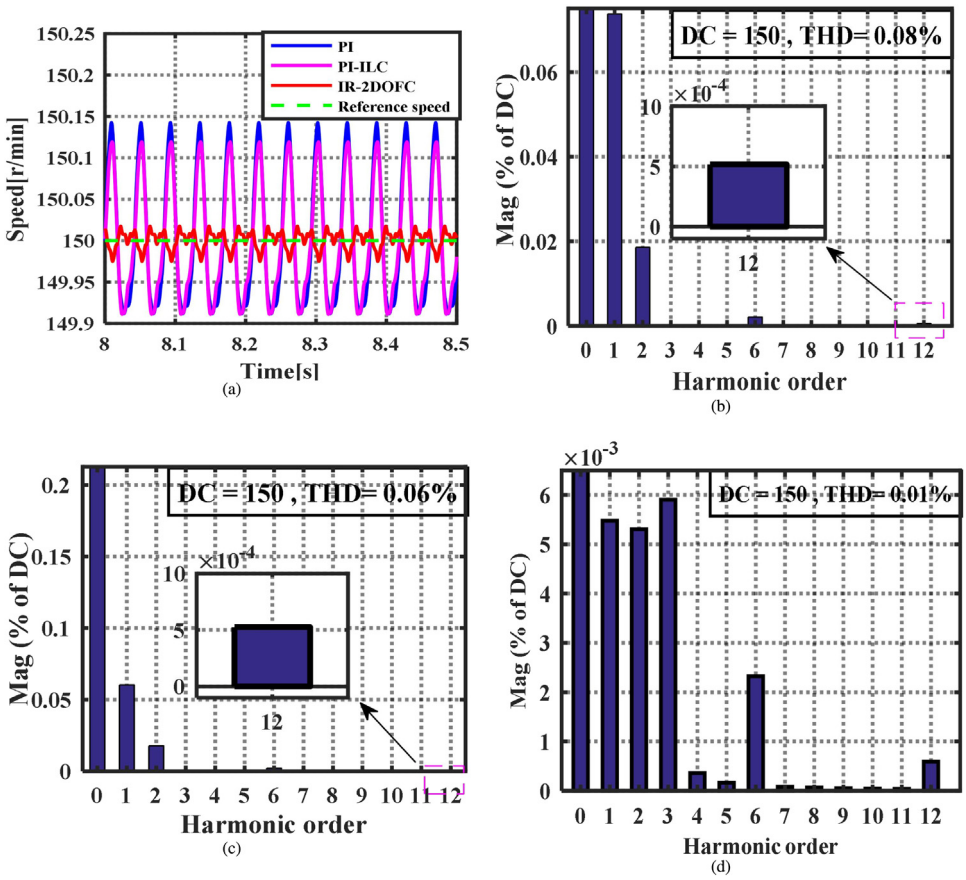

Fig. 9. Simulation results of speed and FFT analyses with three control methods: (a) speed comparisons with PI, PI-ILC, and IR-2DOFC; (b) FFT analysis of the speed with PI controller; (c) FFT analysis of the speed with PI-ILC; (d) FFT analysis of the speed with IR-2DOFC.

5.1.4. Torque ripple suppression performance

The torque ripple is a function of the mechanical angle θ_m; thus, to simulate the actual torque ripple in the PMSM, the following harmonic torques T_h, were injected into the control loop, given by

$$T_h = 0.2sin(\theta_m) + 0.1sin(2\theta_m) + 0.034sin(6\theta_m) + 0.017sin(12\theta_m)\ \text{N m} \quad (52)$$

The fast Fourier transform (FFT) was used to analyze the effect of the torque ripple on speed and output torque. Fig. 9(a) illustrates the steady-state performance of the speed with three control methods. It can be seen that the speed ripples comprised the 1st, 2nd, 6th, and 12th components, and their frequencies were the same as that of the torque ripples. From the FFT analysis, the amplitudes of the 1st, 2nd, 6th, and 12th components with the PI controller were 0.1105, 0.02781, 0.0031, and 7.98×10^{-4} rpm respectively. The total harmonic distortion (THD) index was used to evaluate the speed and torque quality, which is expressed as

$$THD = \sqrt{\sum_{i=1}^{n}\left(\frac{A_i}{A_{DC}}\right)^2} = \sqrt{\sum_{i=1}^{n}(R)^2/100^2} \quad (53)$$

where A_i and A_{DC} represent the amplitudes of the ith harmonics and DC component, and R is the amplitude percentage of the harmonics relative to the DC component.

According to Eq. (53), the THD of the PI controller was 0.08%, which is pretty large. The speed ripple weakened the steady-state performance, which should have been suppressed by the high-performance drive system. Fig. 9(b) illustrates the FFT analysis with PI-ILC, demonstrating that the amplitudes of the 1st and 2nd harmonics were reduced to 0.0969 and 0.02707 rpm, respectively. Meanwhile, the 6th and 12th components were decreased to 0.00298 and 7.83×10^{-4} rpm. The THD was reduced to 0.06%. The quality of the speed was improved to some degree. However, the harmonic amplitude was still large. When the IR-2DOFC was employed in the speed loop, the speed steady-state performance was further improved, and the 1st, 2nd, 6th, and 12th components were decreased to 0.0082, 0.00796, 0.0035, and 6.8×10^{-4} rpm, respectively. The THD was decreased to 0.01%.

Fig. 10 illustrates the simulation results of the output torque and the FFT analysis with the aforementioned control strategies. The amplitudes of the harmonic torque corresponding to the 1st, 2nd, 6th and 12th PI controllers were 0.198, 0.100, 0.0334, and 0.0168 N m, respectively. It is worth noting that the amplitudes of these harmonic torques were near the amplitude of the injected harmonic torque. Therefore, we can conclude that the pure PI controller had limited ability to reject the torque ripple of a real drive system. When the PI-ILC controller was used, the output torque was enhanced, and the 1st, 2nd, 6th, and 12th amplitudes dropped to 0.163, 0.0957, 0.0328, and 0.0166 N m, respectively. The torque ripple with the PI-ILC was decreased by 14.75%, but it was still large. Through a comparison of the PI and the PI-ILC, the IR-2DOFC effectively suppressed the torque ripple, and their harmonic components decreased to 0.014, 0.028, 0.0311, and 0.0158 N m, respectively. It was observed that the IR-2DOFC had better torque-ripple suppression compared with the PI and PI-ILC controllers. The simulation results of the speed and output torque are summarized in Table 2.

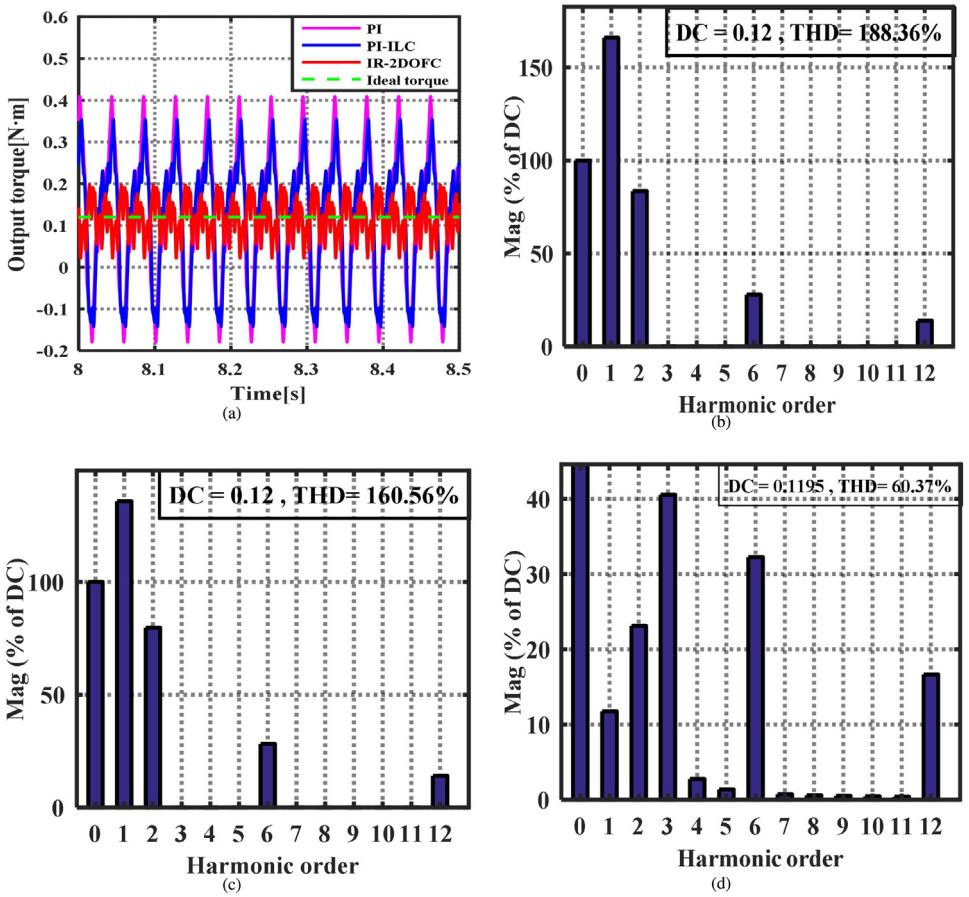

Fig. 10. Simulation results of the output torque and FFT analysis with three control methods: (a) output torque comparisons with PI, PI-ILC, and IR-2DOFC; (b) FFT analysis of the output torque with a PI controller; (c) FFT analysis of the output torque with PI-ILC; (d) FFT analysis of the output torque with IR-2DOFC.

Table 2
Simulation results of the three control methods.

Harmonic order		1st	2nd	6th	12th	THD (%)
Speed (rpm)	PI	0.1105	0.02781	0.0031	$7.9\ 8\times10^{-4}$	0.08
	PI-ILC	0.0969	0.02707	0.00298	7.83×10^{-4}	0.06
	IR-2DOFC	0.0082	0.00796	0.0035	6.8×10^{-4}	0.01
Output torque (N m)	PI	0.198	0.1	0.0334	0.0168	188.36
	PI-ILC	0.163	0.0957	0.0328	0.0166	160.56
	IR-2DOFC	0.014	0.028	0.0311	0.0158	60.37

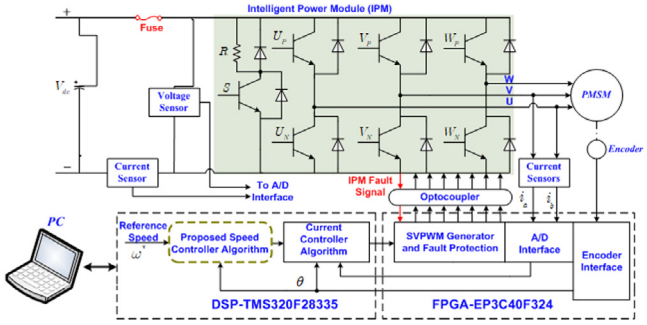

Fig. 11. Structural diagram of the PMSM servo system.

Fig. 12. PMSM servo system setups.

5.2. Experiments verification

To validate the effectiveness of the proposed control strategy in a real drive system, the experiments were carried out using DSP-TMS320F28335 and FPGA-EP3C40F324-based hardware platforms. The digital signal processing (DSP) was adopted to realize the algorithms of the proposed controller and the space-vector pulse-width modulation. A field-programmable gate array (FPGA) was used to generate the control signals of the insulated-gate bipolar transistor that would receive the code value from the encoder. The bus voltage of the inverter was 48 V, and the sampling frequency of the speed loop was set to 1000 Hz. The PMSM control structural diagram and setups are illustrated in Figs. 11 and 12, respectively. The PMSM parameters that were used are listed in Table 1.

5.2.1. Parameter estimation

Fig. 13(a) presents the estimation result of inertia using ESMPO; it can be seen that inertia J, can be identified when different accelerations are adopted. From the experimental results, it can be seen that the estimated value of ESMPO converged to 0.11 kg m^2. Fig. 13(b) presents the estimation results for the viscous friction coefficient B, which ensures that the motor runs

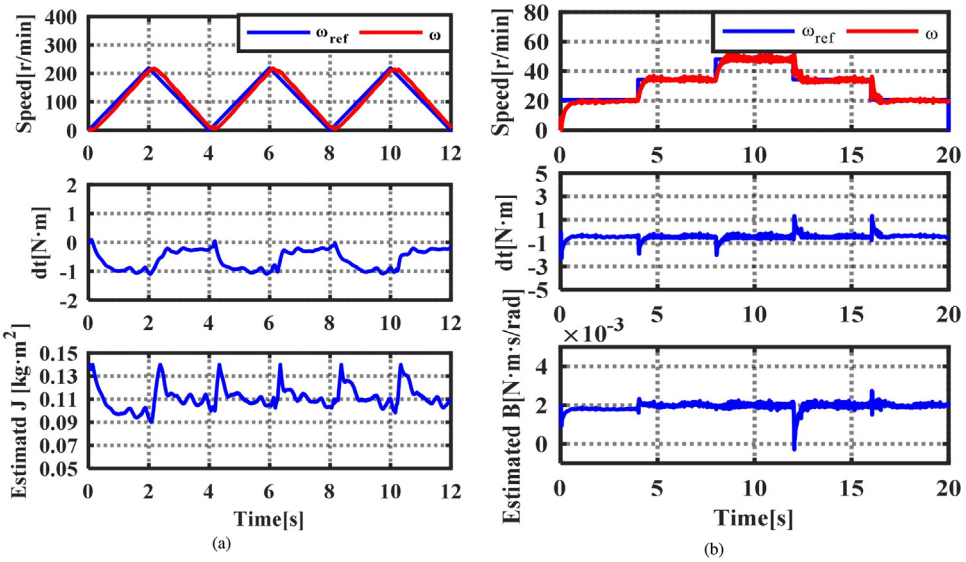

Fig. 13. PMSM servo system setups.

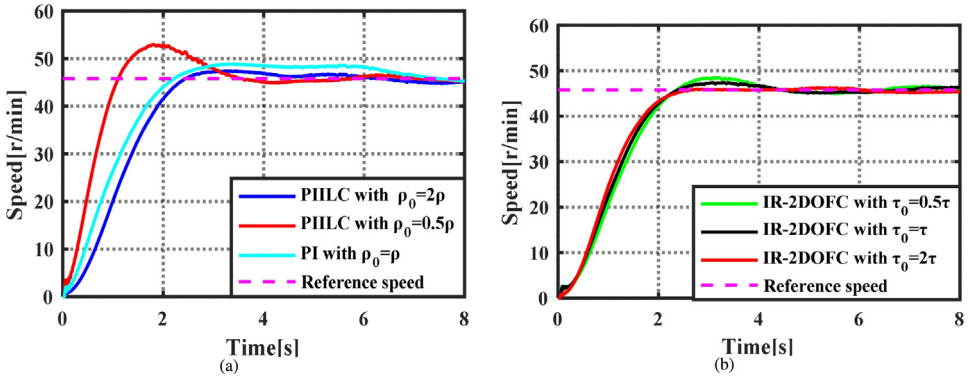

Fig. 14. Experimental results of step response evaluation of PI-ILC and IR-2DOF-IMC: (a) step response of PI-ILC with different values of ρ_0; (b) step response of IR-2DOFC with different constant values of τ.

at varying speeds with zero acceleration. The estimated value finally converges to 0.0023 N m s/rad. The estimated mechanism parameter of the motor is employed to design the optimal PI controller and IR-2DOFC. Meanwhile, the disturbance can be observed in the two testing conditions, indicating that the estimated load torque can be utilized as a disturbance compensation technique for the speed loop.

5.2.2. Dynamic response evaluation

Fig. 14 exhibits the dynamic response of parameter tuning results with PI, PI-ILC, and IR-2DOFC. As can be seen in Fig. 14(a), the transition process having an optimal PI controller can track the given value, and the maximum overshoot reaches 8.6%. When the PI-ILC controller is used in the speed controller, a larger overshoot with 17.5% is produced in the dynamic response, producing a larger settling time for the PI velocity controller. The overshoot can be decreased by setting a smaller time constant ρ. However, the bandwidth is reduced. Through a comparison thereof with the PI-ILC, the proposed IR-2DOFC exhibits better transition performance. It can be seen from Fig. 14(b) that the dynamic response with IR-2DOFC can improve the dynamic response while maintaining a fixed settling time. When parameter τ_0 tunes to 2τ, the overshoot drops to a value of 2.05%. It is thus obvious that the proposed IR-2DOFC can guarantee better transition regulation performance compared with PI and PI-ILC velocity controllers.

5.2.3. Disturbance suppression evaluation with external load

To verify the effectiveness of the disturbance rejection performance of the IR-2DOFC, an external load of 1.2 N m is acted upon the motor when it is operated in a steady state. As can be seen from Fig. 15, the load disturbance results in a maximum steady-state error of 9.4 rpm when the PI controller is used. Through combination of the ESMPO and PI controller, the maximum steady-state error decreases to 7.28 rpm. It is apparent that the ESMPO contributes to the compensation of disturbances, and it improves the disturbance rejection for external loads. When the proposed control method was employed in a speed loop, the maximum steady-state error further reduced to 6.62 rpm. Meanwhile, the time required to return to steady state was smaller than that of pure and ESMPO-based PI controllers. Hence, the proposed controller can achieve satisfactory disturbance suppression performance for external loads, and the effectiveness of the proposed controller is validated.

5.2.4. Torque ripple suppression performance

To analyze the components of speed ripple, the data from the steady-state period of 20–35 s was employed to obtain the THD values caused by the 1st, 2nd, 6th and 12th harmonics torques, and the speed waveform is illustrated in Fig. 16(a). According to the FFT analysis, the amplitudes of the 1st, 2nd, 6th, and 12th speed ripples with the PI controller were 0.956, 0.0543, 0.0378, and 0.0274 rpm, respectively, and the DC component was 44.64

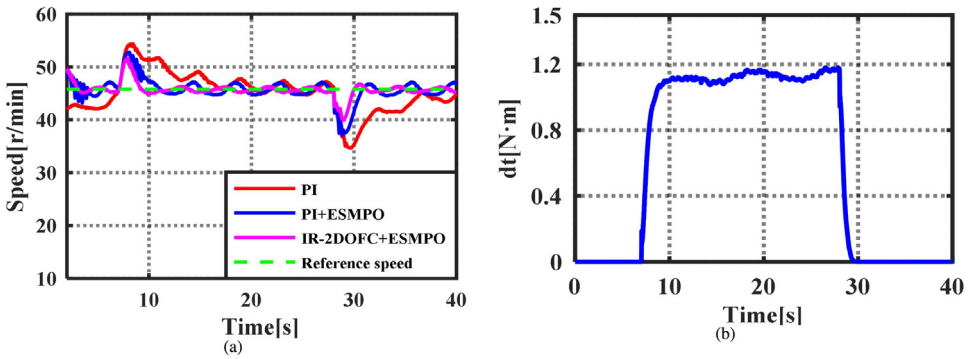

Fig. 15. Experimental results of the disturbance rejection performance: (a) speed steady-state performance with sudden load; (b) curves of observed load disturbance with ESMPO.

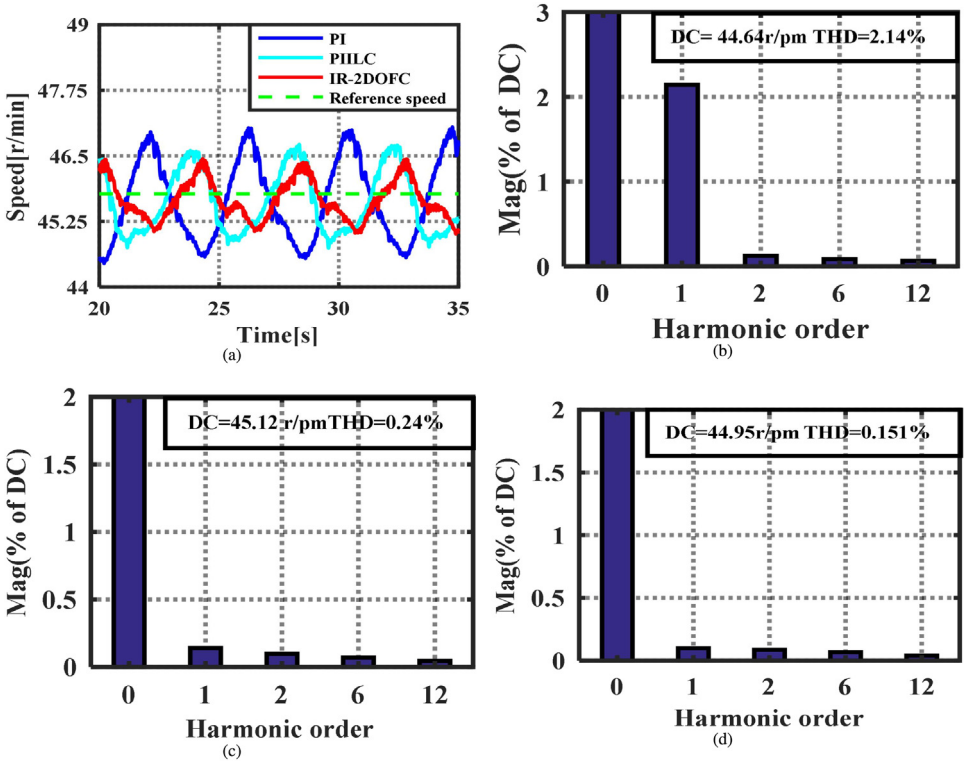

Fig. 16. Experimental results of speed ripple with PI controller, PI-ILC, and IR-2DOFC. (a) Actual speed curves with three controllers. (b) FFT analysis of speed with PI controller. (c) FFT analysis of speed with PI-ILC. (d) FFT analysis of speed with IR-2DOFC.

rpm. Additionally, the THD reached a value of 2.14%. When the PI-ILC speed controller was used, these harmonic components decreased to 0.063 (1st), 0.044 (2nd), 0.031 (6th), and 0.0204 rpm (12th), respectively. The DC component was 45.12, and the THD reduced by 88.78% compared with the PI controller. When the proposed IR-2DOC was utilized, the 1st, 2nd, 6th, and 12th harmonics were further decreased by 95.39%, 41.97%, 21.43%, and 38.19%, respectively. The DC speed value was 44.95 rpm, and the THD decreased to 0.151%.

Fig. 17 demonstrates the output torque curves from three control methods and their FFT analyses. It can be seen from Fig. 17(a) that the output torque with the PI controller shows a large harmonic torque. The DC torque is 0.43 N m, and the 1st, 2nd, 6th, and 12th harmonic contents are 0.031, 0.0224, 0.021, and 0.0198 N m, respectively. The THD reached a value of 11.14%, which is quite large. When the PI-ILC is used for the speed loop, the 1st, 2nd, 6th, and 12th harmonic components decreased to 0.0302, 0.021, 0.019, and 0.0176 N m. The DC component was 0.425 N m, and the THD decreased to 10.56%. Fig. 17(d) exhibits the FFT analysis of the output torque with the proposed IR-2DOFC, it can be observed that the DC torque was 0.3826 N m, and the THD values dropped to 8.9%. The 1st, 2nd, 6th, and 12th harmonic torques were reduced to 0.0265, 0.0154, 0.0125, and 0.0078 N m, respectively. It can be concluded that the proposed controller provides a better torque ripple suppression performance in comparison with PI and PI-ILC. These experimental results are concluded in Table 3.

6. Conclusion

This paper proposed an enhanced robust 2DOFC that utilizes a series-connected ILC and an ESMPO to attenuate the torque ripples and the unmodeled disturbances of the speed loop. The 2DOFC was designed to improve the dynamic response that is otherwise weakened by the ILC and guarantee certain robustness to the disturbance in speed loop. The ILC having a series

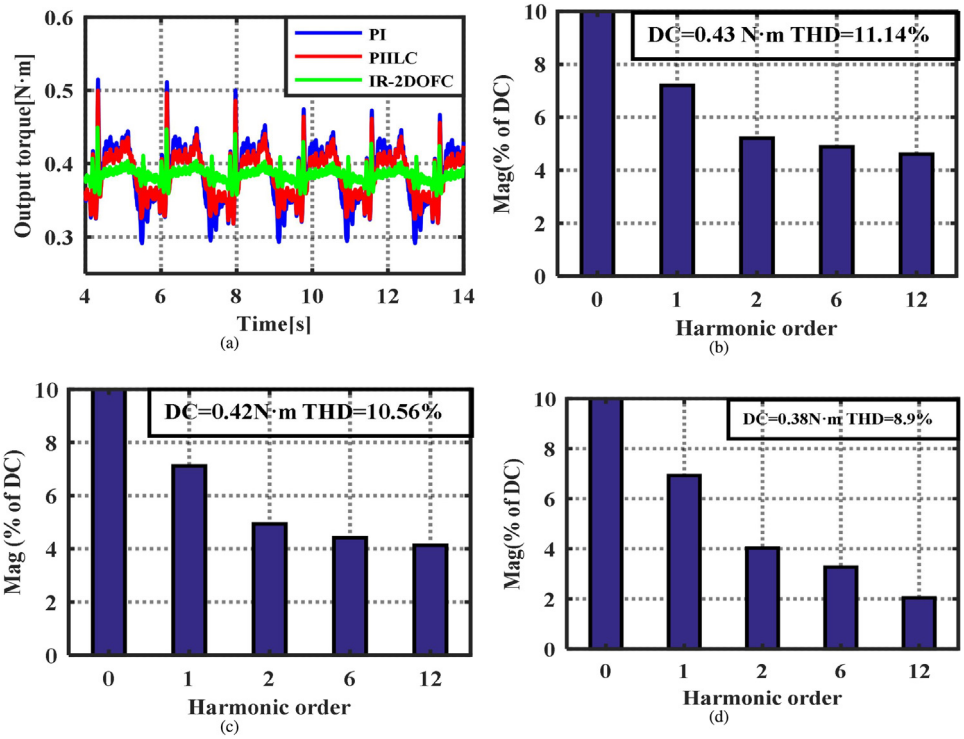

Fig. 17. Experimental results of the output torque and FFT analysis with three control methods: (a) output torque with control methods; (b) FFT analysis of the output torque with PI controller; (c) FFT analysis of the output torque with PI-ILC; (d) FFT analysis of the output torque with IR-2DOFC.

Table 3
Experimental results of the three control methods.

Harmonic order		1st	2nd	6th	12th	THD (%)
Speed (rpm)	PI	0.956	0.0543	0.0378	0.0274	2.14
	PI-ILC	0.063	0.044	0.031	0.0204	0.24
	IR-2DOFC	0.044	0.0386	0.0297	0.0178	0.151
Output torque (N m)	PI	0.031	0.0224	0.021	0.0198	11.14
	PI-ILC	0.0302	0.021	0.019	0.0176	10.56
	IR-2DOFC	0.0265	0.0154	0.0125	0.0078	8.9

connection control structure was used to suppress the periodic disturbance resulting from the electrical and mechanical factors. To reduce the model errors and to ensure the robust stability of the IR-2DOFC, the ESMPO was established, which not only estimates the mechanical parameters but also decreases the impact of multiple-source disturbances on the steady-state performance. The proposed method has the potential for application to PMSM systems with torque ripple and parameter variations, particularly for the cases where the inertial and viscous friction parameters of the motor drive systems should be estimated on line.

Declaration of competing interest

The authors declare that they have no known competing financial interests or personal relationships that could have appeared to influence the work reported in this paper.

Acknowledgments

This work is supported by the National Natural Science Foundation of China (Grant no. 11973041 and 12122304), Youth Innovation Promotion Association, China, Chinese Academy of Science (Grant no. 2019218).

References

[1] Wang L, Zhu ZQ, Bin H, Gong LM. Current harmonics suppression strategy for PMSM with nonsinusoidal back-EMF based on adaptive linear neuron method. IEEE Trans Ind Electron 2020;67(11):9164–73.
[2] Bu F, Yang Z, Gao Y, Pan Z, Pu T, Degano M, Gerada C. Speed ripple reduction of direct-drive PMSM servo system at low-speed operation using virtual cogging torque control method. IEEE Trans Ind Electron 2021;68(1):160–74.
[3] Hou Q, Ding S, Yu X. Composite super-twisting sliding mode control design for PMSM speed regulation problem based on a novel disturbance observer. IEEE Trans Energy Convers 2020;36(4):2591–9.
[4] Zhang Y, Jin J, Huang L. Model-free predictive current control of PMSM drives based on extended state observer using ultralocal model. IEEE Trans Ind Electron 2021;68(2):993–1003.
[5] Deng Y, Wang J, Li H, Liu J, Tian D. Adaptive sliding mode current control with sliding mode disturbance observer for PMSM drives. ISA Trans 2019;88:113–26.
[6] Wang G, Hu H, Ding D, Zhao N, Zou Y, Xu D. Overmodulation strategy for electrolytic capacitorless PMSM drives: Voltage distortion analysis and boundary optimization. IEEE Trans Power Electron 2020;35(9):9576–87.
[7] Zhang X, Zhang L, Zhang Y. Model predictive current control for PMSM drives with parameter robustness improvement. IEEE Trans Power Electron 2019;34(2):1645–57.
[8] Young HA, Perez MA, Rodriguez J. Analysis of finite-control-set model predictive current control with model parameter mismatch in a three-phase inverter. IEEE Trans Ind Electron 2016;63(5):3100–7.
[9] Fuentes EJ, Silva CA, Yuz JI. Predictive speed control of a two-mass system driven by a permanent magnet synchronous motor. IEEE Trans Ind Electron 2012;59(7):2840–8.
[10] Han J. From PID to active disturbance rejection control. IEEE Trans Ind Electron 2009;56(3):900–6.
[11] Mynar Z, Vesely L, Vaclavek P. PMSM model predictive control with field-weakening implementation. IEEE Trans Ind Electron 2016;63(8):5156–66.
[12] Luo Y, Liu C. Model predictive control for a six-phase PMSM motor with a reduced-dimension cost function. IEEE Trans Ind Electron 2020;67(2):969–79.
[13] Han Y, Gong C, Yan L, Wen H, Wang Y, Shen K. Multiobjective finite control set model predictive control using novel delay compensation technique for PMSM. IEEE Trans Power Electron 2020;35(10):11193–204.
[14] Hou S, Fei J, Chen C, Chu Y. Finite-time adaptive fuzzy-neural-network control of active power filter. IEEE Trans Power Electron 2019;34(10):10298–313.

[15] Bu X, Xiao Y, Lei H. An adaptive critic design-based fuzzy neural controller for hypersonic vehicles: Predefined behavioral nonaffine control. IEEE-ASME Trans Mechatron 2020;24(4):1871–81.
[16] Hang J, Wu H, Zhang J, Ding S, Huang Y, Hua W. Cost function-based open-phase fault diagnosis for PMSM drive system with model predictive current control. IEEE Trans Power Electron 2021;36(3):2574–83.
[17] Choi HH, Vu NTT, Jung JW. Digital implementation of an adaptive speed regulator for a PMSM. IEEE Trans Power Electron 2011;26(1):3–8.
[18] Chen W-H, Yang J, Guo L, Li S. Disturbance-observer-based control and related methods—An overview. IEEE Trans Ind Electron 2016;63(2):1083–95.
[19] Sun L, Zhang X, Sun L, Zhao K. Nonlinear speed control for PMSM system using sliding-mode control and disturbance compensation techniques. IEEE Trans Power Electron 2013;28(3):1358–65.
[20] Guo T, Sun Z, Wang X, Li S, Zhang K. A simple current-constrained controller for permanent-magnet synchronous motor. IEEE Trans Ind Inf 2019;15(3):1486–95.
[21] Umeno T, Hori Y. Robust speed control of DC servomotors using modern two degrees-of-freedom controller design. IEEE Trans Ind Electron 1991;38(5):363–8.
[22] Li P, Zhu G. Robust internal model control of servo motor based on sliding mode control approach. ISA Trans 2019;93:199–208.
[23] Tan W. Analysis and design of a double two-degree-of-freedom control scheme. ISA Trans 2010;49(3):311–7.
[24] Ajmeri M, Ali A. Two degree of freedom control scheme for unstable processes with small time delay. ISA Trans 2015;56:308–26.
[25] Gan WC, Qiu L. Torque and velocity ripple elimination of AC permanent magnet motor control systems using the internal model principle. IEEE-ASME Trans Mechatron 2004;9(2):436–47.
[26] Mendoza-Mondragon F, Hernandez-Guzman VM, Rodriguez-Resendiz J. Robust speed control of permanent magnet synchronous motors using two-degrees-of-freedom control. IEEE Trans Ind Electron 2018;65(8):6099–108.
[27] Araki M, Taguchi H. Two-degree-of-freedom PID controllers. Int J Control Autom Syst 2003;1(4):401–11.
[28] Xia C, Ji B, Yan Y. Smooth speed control for low-speed high-torque permanent-magnet synchronous motor using proportional-integral-resonant controller. IEEE Trans Ind Electron 2015;62(4):2123–34.
[29] Yan Y, Yang J, Sun Z, Zhang C, Li S, Yu H. Robust speed regulation for PMSM servo system with multiple sources of disturbances via an augmented disturbance observer. IEEE-ASME Trans Mechatron 2018;23(2):769–80.
[30] Zanchetta P, Degano M, Liu J, Mattavelli P. Iterative learning control with variable sampling frequency for current control of grid-connected converters in aircraft power systems. IEEE Trans Ind Appl 2013;49(4):1548–55.
[31] Simba KR, Bui BD, Msukwa MR, Uchiyama N. Robust iterative learning contouring controller with disturbance observer for machine tool feed drives. ISA Trans 2018;75:207–15.
[32] Zhang W, Cao B, Nan N, Li M, Chen YQ. An adaptive PID-type sliding mode learning compensation of torque ripple in PMSM position servo systems towards energy efficiency. ISA Trans 2021;110:258–70.
[33] Qian W, Panda SK, Xu JX. Speed ripple minimization in PM synchronous motor using iterative learning control. IEEE Trans Energy Convers 2005;20(1):53–61.
[34] Zhu Q, Song F, Xu JX, Liu Y. An internal model based iterative learning control for wafer scanner systems. IEEE-ASME Trans Mechatron 2019;24(5):2073–84.
[35] Toloue SF, Moallem M. Torque control of a brushless DC motor using multivariable sliding mode extremum seeking PI tuning. In: Proceedings IECON 2017 - 43rd annual conference of the IEEE industrial electronics society, Vol. 2017-January. 2017, p. 2917–22. http://dx.doi.org/10.1109/IECON.2017.8216492.
[36] Toloue SF, Kamali SH, Moallem M. Torque ripple minimization and control of a permanent magnet synchronous motor using multiobjective extremum seeking. IEEE-ASME Trans Mechatron 2019;24(5):2151–60.
[37] Xia C, Deng W, Shi T, Yan Y. Torque ripple minimization of PMSM using parameter optimization based iterative learning control. J Electr Eng Technol 2016;11(2):425–36.
[38] Fei Q, Deng Y, Li H, Liu J, Shao M. Speed ripple minimization of permanent magnet synchronous motor based on model predictive and iterative learning controls. IEEE Access 2019;7:31791–800.
[39] Liu J, Li H, Deng Y. Torque ripple minimization of PMSM based on robust ILC via adaptive sliding mode control. IEEE Trans Power Electron 2018;33(4):3655–71.
[40] Yuan X, Zhang S, Zhang C. Enhanced robust deadbeat predictive current control for PMSM drives. IEEE Access 2019;7:148218–30.
[41] Desoer CA, Vidyasagar M. Feedback systems: Input-output properties. Academic; 1975.
[42] Zhang X, Li Z. Sliding-mode observer-based mechanical parameter estimation for permanent magnet synchronous motor. IEEE Trans Power Electron 2016;31(8):5732–45.